

---

# Godunov Loss Functions for Modelling of Hyperbolic Conservation Laws

---

**Rami Cassia**

DAMTP

University of Cambridge  
Wilberforce Rd, CB3 0WA  
rgc38@cam.ac.uk

**Rich Kerswell**

DAMTP

University of Cambridge  
Wilberforce Rd, CB3 0WA  
rrk26@cam.ac.uk

## Abstract

Machine learning techniques are being used as an alternative to traditional numerical discretization methods for solving hyperbolic partial differential equations (PDEs) relevant to fluid flow. Whilst numerical methods are higher fidelity, they are computationally expensive. Machine learning methods on the other hand are lower fidelity but provide significant speed-ups. The emergence of physics-informed neural networks (PINNs) in fluid dynamics has allowed scientists to directly use PDEs for evaluating loss functions in an unsupervised manner. The downfall of this approach is that the differential form of systems is invalid at regions of shock inherent in hyperbolic PDEs such as the compressible Euler equations. To circumvent this problem we propose a modification to PDE-based PINN losses by using a finite volume-based loss function that incorporates the flux of Godunov-type methods. These Godunov-type methods are also known as approximate Riemann solvers and evaluate intercell fluxes in an entropy-satisfying manner, yielding more physically accurate shocks. Our approach increases fidelity compared to using regularized PDE-based PINN losses, as tested on the 2D Riemann problem.

## 1 Introduction

Machine learning (ML) has become an increasingly popular tool in computational fluid dynamics (CFD). Applications broadly fall into the areas of CFD acceleration [1, 2, 3], reduced-order modelling (ROM) [4, 5, 6], turbulence modelling [7, 8, 9], active flow control [10, 11, 12] and flow reconstruction [13, 14, 15]. In this work we are interested in using ML to model compressible flows governed by hyperbolic partial differential equations (PDEs). ML models in this context must ensure predictions are entropy-satisfying and prevent artificial oscillations forming in the flow.

Raissi et al. [16] propose an unsupervised method of integrating physics into ML frameworks by including physics-based PDE losses rather than using standard ML losses. They demonstrate the feasibility of these physics-informed neural networks (PINNs) on Navier-Stokes, Korteweg-De Vries, and Burgers' equations. The use of PINNs for modelling of physical phenomena has gained popularity in recent times, particularly in fluid dynamics. This is in part due to the added interpretability that physical losses bring to ML. Numerous architectural modifications to standard fully-connected PINNs (FC-PINNs) have been proposed. For example, Ren et al. [17] use a convolutional long short-term memory network (Conv-LSTM) with hard imposition of initial/boundary conditions (I/BCs) to model the viscous 2D Burgers' equations. Their work demonstrates improvement over FC-PINNs due to the ability of convolutional LSTMs in capturing spatiotemporal flow features. The hard imposition of I/BCs via padding negates the use of penalty terms which reduces hyperparameter tuning. Autoregressive and residual connections of the architecture also simulate time marching. The limitation of using PDE-based PINN losses for hyperbolic systems is their invalidity in potential

shock regions. Mao et al. [18] alleviate this limitation by clustering training points in regions where shocks develop. This however requires prior knowledge of shock location. Liu et al. [19] introduce an additional loss term that is a function of flow gradient, such that highly-compressed regions have a smaller weighting during loss evaluation. The methodology is used to simulate the 2D Riemann problem as governed by the compressible Euler equations. Their method improves performance of PDE-based losses and yields accuracy comparable with high-order numerical methods.

Further feasible ideas for ML modelling of conservative hyperbolic systems can be drawn from traditional numerical techniques. As such we briefly review these techniques. The first major advancement in finite volume methods (FVMs) for compressible flows and hyperbolic systems can be traced back to the work of Godunov in 1959 [20]. The so-called Godunov scheme assumes the flow-field is piecewise constant and relies on the exact solution of the local Riemann problem at each cell interface to estimate the intercell fluxes [21]. Godunov's scheme preserves monotonicity and is entropy-satisfying [22]. However, Godunov's theorem states that monotonicity-preserving constant-coefficient schemes can be at most 1st-order accurate [20]. Since the Riemann problem has to be exactly solved at every interface and at every time step, the Godunov scheme is computationally expensive when applied to non-linear systems of conservation laws [22]. Nevertheless the work of Godunov inspired the development of numerous extensions to his scheme. These extensions focus on reducing computational burden by approximating the Riemann problem or the flux computation. Such schemes are known as approximate Riemann solvers. One such scheme developed by Roe [23] linearizes the quasi-linear form of hyperbolic conservative equations by replacing Jacobians with interval-wise constant matrices such that hyperbolicity, consistency, and conservation are still satisfied. The approximate Riemann problem is linear meaning solutions only admit discontinuities and not expansion fans. Roe's method is therefore not entropy-satisfying although entropy fixes have been proposed [24]. Osher's method is similar to Roe's method but approximates the Riemann problem using simple waves, rather than discontinuities [25, 26]. Osher's method is entropy-satisfying [22]. The methods of Roe and Osher assume  $n$  intermediate states for  $n$  conservation laws when approximating the Riemann problem. Harten et al. [27] propose a simplification by assuming a Riemann solution of three states separated by two waves, which correspond to the fastest and slowest signal speeds emerging from the discontinuity at a cell interface. They name their algorithm the Harten, Lax, Van Leer solver (HLL). Toro et al. [28] modify the HLL solver by assuming an additional middle wave that accounts for contact and shear waves, known as the HLLC solver. Both HLL and HLLC are entropy-satisfying [22].

Godunov's theorem led to much research on developing higher-order non-linear schemes applicable to hyperbolic systems. Harten [29] postulates that monotonicity-preserving higher-order schemes are achievable provided the discrete total variation (TV) of the solution does not increase over time. He coins schemes that satisfy this non-increase in TV as total variation diminishing (TVD). The monotonic upstream-centered scheme for conservation laws (MUSCL) reconstructs piece-wise constant data into piecewise linear data to achieve 2nd-order accuracy [30, 31]. The reconstruction includes slope-limiting techniques to ensure the scheme is TVD. Similarly the piecewise parabolic method (PPM) is of 3rd-order accuracy [32, 33]. Essentially non-oscillatory schemes (ENO) involve a recursive piecewise polynomial reconstruction to the desired order of accuracy by iteratively including stencils for interpolation [34, 35, 36, 37, 38]. The choice between candidate stencils is based on which provides the smoothest interpolation as indicated by smoothness indicators. ENO is not strictly TVD although oscillations tend to disappear if the solution is adequately resolved [22]. WENO is a TVD-extension of ENO that uses a weighted convex combination of all possible candidate stencils for reconstruction [39]. Both ENO and WENO can achieve up to 5th-order accuracy. For a more detailed discussion of FVMs for hyperbolic systems we refer the reader to [40, 21].

ML research that draws from traditional numerical techniques is as follows. Patel et al. [41] use a control volume PINN (cvPINN) which evaluates the physics-informed loss in integral form rather than PDE form. They use artificial viscosity and an entropy inequality penalization term to yield entropy-satisfying solutions. A TV penalization term is also used to prevent artificial oscillations developing in the solution. Their method proves to be superior to standard PDE-based PINNs when modelling 1D Euler and Bucky-Leverett equations. The use of three additional terms however leads to additional hyperparameter tuning. It is also unclear how the intercell flux is calculated in evaluating the control volume loss. Bezgin et al. [42] use a neural network to optimize the artificial viscosity parameter in the Lax-Friedrichs flux to yield a stable and less diffusive solution for the 2D Riemann

problem. Xiong et al. [43] use convolutional neural networks (CNNs) to predict the linearization matrices of the Roe solver from the flow solution to perform time-stepping. Their method improves over a traditional Roe solver when applied on the shock-tube problem. Kossaczka et al. [44, 45] use neural networks to optimize the smoothness indicators of WENO schemes. They also add a regularization term to a MSE loss to penalize any overflows of the solution, thereby preventing artificial oscillations. Their method improves over other WENO variants when tested on numerous hyperbolic problems. Other similar works using ML to predict WENO weights and smoothness indicators are [46, 47, 48]. Wang and Hickey [49] make use of Rankine-Hugoniot (R-H) jump conditions to derive a regularizing term. The R-H conditions describe how physical quantities change across a shock wave as derived from conservation laws, eliminating entropy violations. They apply the methodology to simulate the 2D Riemann problem and yield higher accuracy in comparison to a numerical Roe solver.

In this paper, we present the first use of Godunov-type losses for modelling of 2D hyperbolic systems. We define Godunov-type losses as FVM-based loss functions that fundamentally incorporate the approximate solution of the Riemann problem to estimate the intercell fluxes required in the control volume loss. In using such loss functions we hope to a) improve accuracy compared to regularized PDE-based PINNs and b) encourage entropy-satisfying non-oscillatory solutions without regularization terms (that otherwise require tuning). Like PINNs, our approach is unsupervised. We use this loss function to train a Conv-LSTM model to time-step the 2D Riemann problem as governed by the 2D Euler equations. The 2D Riemann problem gives rise to varying complex flow patterns for different initial conditions (or configurations) and thus serves as a common canonical problem for testing compressible flow solvers. To estimate the fluxes in the FVM-based loss we use the HLLC approximate Riemann solver. We time-step six different configurations of the 2D Riemann problem, indicating generalizability and robustness to various initial conditions. We show that the Godunov-type loss outperforms PDE-based losses with additional viscous, TV and entropy regularization terms used by Patel et al. [41] and Ren et al. [17].

The paper is structured as follows: in Section 2 we outline the equations, the Conv-LSTM architecture, the formulation of the Godunov-type loss and its HLLC flux estimation. In Section 3 we outline the experimental setup and discuss results. Finally we make concluding remarks in Section 4.

## 2 Methodology

### 2.1 Equations

We are interested in conservative hyperbolic PDEs of the general form:

$$\partial_t \mathbf{Q} + \partial_x \mathbf{F}(\mathbf{Q}) + \partial_y \mathbf{G}(\mathbf{Q}) + \partial_z \mathbf{H}(\mathbf{Q}) = \mathbf{0}, \quad (1)$$

with associated boundary conditions (BCs), where  $\mathbf{Q}$  is the vector of conserved quantities and  $\mathbf{F}$ ,  $\mathbf{G}$  and  $\mathbf{H}$  are the flux vectors in the  $x$ ,  $y$  and  $z$  directions. Re-writing equation (1) in quasilinear form:

$$\partial_t \mathbf{Q} + \partial_{\mathbf{Q}} \mathbf{F} \partial \mathbf{Q}_x + \partial_{\mathbf{Q}} \mathbf{G} \partial \mathbf{Q}_y + \partial_{\mathbf{Q}} \mathbf{H} \partial \mathbf{Q}_z = \mathbf{0}, \quad (2)$$

allows us to define a hyperbolic system.

**Definition** [21]: A system is said to be hyperbolic at any point in space and time if the eigenvalues of Jacobians  $\partial_{\mathbf{Q}} \mathbf{F}$ ,  $\partial_{\mathbf{Q}} \mathbf{G}$ , and  $\partial_{\mathbf{Q}} \mathbf{H}$  are all real with a corresponding set of linearly independent eigenvectors. The system is said to be strictly hyperbolic if the eigenvalues are distinct.

In this paper we focus particularly on the 2D Euler equations:

$$\partial_t \begin{pmatrix} \rho \\ \rho u \\ \rho v \\ E \end{pmatrix} + \partial_x \begin{pmatrix} \rho u \\ \rho u^2 + p \\ \rho uv \\ u(E + p) \end{pmatrix} + \partial_y \begin{pmatrix} \rho v \\ \rho uv \\ \rho v^2 + p \\ v(E + p) \end{pmatrix} = \mathbf{0}, \quad (3)$$

with associated Neumann BCs  $\partial_n \mathbf{Q} = \mathbf{0}$ . To close the system energy  $E$  is expressed in terms of velocities, pressure, density and ratio of specific heats  $\gamma$ :

$$E := \frac{1}{2} (u^2 + v^2) + \frac{p}{\rho(\gamma - 1)}. \quad (4)$$

## 2.2 Architecture

We implement a convolutional LSTM architecture with a global residual connection to mimic the forward Eulerian scheme:

$$\mathbf{X}^{n+1} = \mathbf{X}^n + \Delta \mathbf{X}^n = \mathbf{X}^n + \Delta t \cdot \mathcal{F}(\mathbf{X}^n; \Theta), \quad (5)$$

where  $\mathbf{X}$  is the feature,  $\mathcal{F}$  is the network parameterized by network weights  $\Theta$ ,  $\Delta t$  is the step size, and  $n$  is the temporal index. The residual connection in equation (5) automatically imposes the initial condition of the PDEs of concern. Constant Neumann BCs are embedded into the network architecture by padding with values interpolated from the interior domain. The simplest case, where the BC is  $\partial_n \mathbf{Q} = \mathbf{0}$ , is incorporated using replicative padding. See Appendix A for further details on the Conv-LSTM architecture. We choose  $\mathbf{X}$  to be the set of primitives  $(\rho, u, v, E)^T$ .

## 2.3 Godunov-type Loss

A standard PINN evaluates its loss by directly evaluating derivatives in the relevant PDEs. However the differential form of the governing equations is invalid in regions of shocks that may manifest in hyperbolic systems. An integral form on the other hand is applicable across shocks. The approach presented here for evaluating the loss function is finite volume-based and inherently aims to achieve three desirable properties. Firstly, the approach aims to satisfy the weak form of the conservation law. In 1D, over domain  $[t_1, t_2] \times [x_1, x_2]$ , the weak conservation law is:

$$\int_{x_1}^{x_2} [\mathbf{Q}(x, t_2) - \mathbf{Q}(x, t_1)] dx + \int_{t_1}^{t_2} [\mathbf{F}(\mathbf{Q}(x_2, t)) - \mathbf{F}(\mathbf{Q}(x_1, t))] dt = \mathbf{0}. \quad (6)$$

Secondly, the approach aims to satisfy the weak form of the entropy condition to encourage physically correct shocks. In 1D, over the same domain, the condition is:

$$\int_{x_1}^{x_2} [\Phi(\mathbf{Q}(x, t_2)) - \Phi(\mathbf{Q}(x, t_1))] dx + \int_{t_1}^{t_2} [\tilde{\mathbf{F}}(\mathbf{Q}(x_2, t)) - \tilde{\mathbf{F}}(\mathbf{Q}(x_1, t))] dt \leq 0, \quad (7)$$

where convex entropy function  $\Phi(\mathbf{Q})$  satisfies  $\partial_{\mathbf{Q}} \Phi \partial_{\mathbf{Q}} \mathbf{F} = \partial_{\mathbf{Q}} \tilde{\mathbf{F}}$ , where  $\tilde{\mathbf{F}}$  is the entropy flux. Thirdly, the approach aims to preserve solution monotonicity (i.e., prevent artificial oscillations). See Section 1 in Harten et al. [27] for a detailed discussion of these three properties. A class of FVMs possessing these properties are known as Godunov methods. In the following subsections we outline the Godunov method then derive our so-called Godunov-type loss from it. Godunov's method is outlined in 1D for brevity but is then extended to 2D before formulating the loss, as we are ultimately interested in modelling the 2D Euler equations.

### 2.3.1 Godunov Methods

Godunov methods are based on solving local Riemann problems at each FVM cell interface. Assuming piecewise-constant  $\mathbf{Q}(x_i, t^n) = \mathbf{Q}_i^n$ , the local Riemann problem at cell interface  $i + 1/2$ , at the  $n$ th time:

$$\mathbf{Q}(\bar{x}, \bar{t} = 0) = \begin{cases} \mathbf{Q}_l \equiv \mathbf{Q}_i^n & \bar{x} < 0, \\ \mathbf{Q}_r \equiv \mathbf{Q}_{i+1}^n & \bar{x} > 0, \end{cases} \quad (8)$$

depends only on states  $\mathbf{Q}_l$  and  $\mathbf{Q}_r$ , and ratio of local coordinates  $\bar{x}/\bar{t}$ , where  $\bar{x} = x - x_{i+1/2}$  and  $\bar{t} = t - t^n$ . Since signals travel with finite velocity bounded by a minimum  $a_l$  and a maximum  $a_r$ , then [27]:

$$\mathbf{Q}(\bar{x}/\bar{t}; \mathbf{Q}_l, \mathbf{Q}_r) = \begin{cases} \mathbf{Q}_l \equiv \mathbf{Q}_i^n & \bar{x}/\bar{t} \leq a_l, \\ \mathbf{Q}_r \equiv \mathbf{Q}_{i+1}^n & \bar{x}/\bar{t} \geq a_r. \end{cases} \quad (9)$$

By assuming  $\lambda |a_{max}| < 1/2$ , where  $a_{max}$  is the largest signal speed in the domain and  $\lambda = \Delta t / \Delta x$ , then by equation (9) there is no interaction between neighbouring Riemann problems and the solution  $\hat{\mathbf{Q}}$  in the interval  $[t^n, t^{n+1}] \times [x_i, x_{i+1}]$  can be expressed exactly in terms of the solution to the local Riemann problem [21]:

$$\hat{\mathbf{Q}}(x, t) = \mathbf{Q}(\bar{x}/\bar{t}; \mathbf{Q}_i^n, \mathbf{Q}_{i+1}^n). \quad (10)$$

A piecewise-constant approximation at the next time  $t^{n+1}$  is then given by:

$$\mathbf{Q}_i^{n+1} = \frac{1}{\Delta x} \int_{x_{i-\frac{1}{2}}}^{x_{i+\frac{1}{2}}} \hat{\mathbf{Q}}(x, t^n + \Delta t) dx, \quad (11)$$

or in terms of local Riemann problems as:

$$\mathbf{Q}_i^{n+1} = \frac{1}{\Delta x} \int_0^{\frac{\Delta x}{2}} \mathbf{Q}(x/\Delta t; \mathbf{Q}_{i-1}^n, \mathbf{Q}_i^n) dx + \frac{1}{\Delta x} \int_{-\frac{\Delta x}{2}}^0 \mathbf{Q}(x/\Delta t; \mathbf{Q}_i^n, \mathbf{Q}_{i+1}^n) dx. \quad (12)$$

If we relax the time-step criterion such that  $\lambda|a_{max}| \leq 1$ , then waves issuing from interface  $x_{i-\frac{1}{2}}$  do not reach  $x_{i+\frac{1}{2}}$  in the interval  $[t^n, t^{n+1}]$ , and vice versa. It can then be shown that, by applying equation (6) over  $[t^n, t^{n+1}] \times [x_{i-\frac{1}{2}}, x_{i+\frac{1}{2}}]$ , we can arrive at a conservative expression at the next time level [27]:

$$\mathbf{Q}_i^{n+1} = \mathbf{Q}_i^n - \lambda \left[ \mathbf{F}(\mathfrak{R})_{i+\frac{1}{2}}^n - \mathbf{F}(\mathfrak{R})_{i-\frac{1}{2}}^n \right], \quad (13)$$

$$\mathbf{F}(\mathfrak{R})_{i+\frac{1}{2}}^n = \mathbf{F}(\mathbf{Q}(\bar{x}/\bar{t} = 0; \mathbf{Q}_i^n, \mathbf{Q}_{i+1}^n)), \quad \mathbf{F}(\mathfrak{R})_{i-\frac{1}{2}}^n = \mathbf{F}(\mathbf{Q}(\bar{x}/\bar{t} = 0; \mathbf{Q}_{i-1}^n, \mathbf{Q}_i^n)). \quad (14)$$

For proof, see Chapter 6 in Toro [21].  $\hat{\mathbf{Q}}$  satisfies the weak form of the entropy condition (inequality (7)):

$$\int_{x_{i-\frac{1}{2}}}^{x_{i+\frac{1}{2}}} \Phi(\hat{\mathbf{Q}}(x, t^n + \Delta t)) dx \leq \Delta \Phi(\mathbf{Q}_i^n) - \Delta t \left[ \tilde{\mathbf{F}}(\mathfrak{R})_{i+\frac{1}{2}}^n - \tilde{\mathbf{F}}(\mathfrak{R})_{i-\frac{1}{2}}^n \right], \quad (15)$$

$$\tilde{\mathbf{F}}(\mathfrak{R})_{i+\frac{1}{2}}^n = \tilde{\mathbf{F}}(\mathbf{Q}(\bar{x}/\bar{t} = 0; \mathbf{Q}_i^n, \mathbf{Q}_{i+1}^n)), \quad \tilde{\mathbf{F}}(\mathfrak{R})_{i-\frac{1}{2}}^n = \tilde{\mathbf{F}}(\mathbf{Q}(\bar{x}/\bar{t} = 0; \mathbf{Q}_{i-1}^n, \mathbf{Q}_i^n)). \quad (16)$$

Since  $\Phi$  is a convex function, we can use Jensen's inequality along with inequality (15) to deduce that Godunov's method satisfies the entropy inequality [27].

Due to averaging in equation (11), information contained in the exact solution of the Riemann problem is lost. This implies more efficient Godunov methods are achievable by assuming a simpler structure to the Riemann solution a-priori. These so-called Godunov-type methods are also known as approximate Riemann solvers. Like Godunov schemes, it can be shown that Godunov-type schemes also satisfy the entropy condition and can be written in conservation form to arrive at equation (13), see Section 3 in Harten et al. [27].

### 2.3.2 Construction of Loss

We are interested in 2D hyperbolic problems, and therefore extend equation (13) to 2D:

$$\mathbf{Q}_{i,j}^{n+1} = \mathbf{Q}_{i,j}^n - \lambda_x \left[ \mathbf{F}(\mathfrak{R})_{i+\frac{1}{2},j}^n - \mathbf{F}(\mathfrak{R})_{i-\frac{1}{2},j}^n \right] - \lambda_y \left[ \mathbf{G}(\mathfrak{R})_{i,j+\frac{1}{2}}^n - \mathbf{G}(\mathfrak{R})_{i,j-\frac{1}{2}}^n \right], \quad (17)$$

where by analogy to equation (14) we can express fluxes  $\mathbf{G}$  as:

$$\mathbf{G}(\mathfrak{R})_{i+\frac{1}{2}}^n = \mathbf{G}(\mathbf{Q}(\bar{y}/\bar{t} = 0; \mathbf{Q}_j^n, \mathbf{Q}_{j+1}^n)), \quad \mathbf{G}(\mathfrak{R})_{i-\frac{1}{2}}^n = \mathbf{G}(\mathbf{Q}(\bar{y}/\bar{t} = 0; \mathbf{Q}_{j-1}^n, \mathbf{Q}_j^n)). \quad (18)$$

For compactness we re-write equation (17) as:

$$\mathbf{Q}_{i,j}^{n+1} = \mathbf{Q}_{i,j}^n - \lambda_x \left[ \Delta \mathbf{F}(\mathfrak{R})_{i,j}^n \right] - \lambda_y \left[ \Delta \mathbf{G}(\mathfrak{R})_{i,j}^n \right], \quad (19)$$

$$\Delta \mathbf{F}(\mathfrak{R})_{i,j}^n = \mathbf{F}(\mathfrak{R})_{i+\frac{1}{2},j}^n - \mathbf{F}(\mathfrak{R})_{i-\frac{1}{2},j}^n, \quad \Delta \mathbf{G}(\mathfrak{R})_{i,j}^n = \mathbf{G}(\mathfrak{R})_{i,j+\frac{1}{2}}^n - \mathbf{G}(\mathfrak{R})_{i,j-\frac{1}{2}}^n, \quad (20)$$

where  $\lambda_x = \Delta t/\Delta x$  and  $\lambda_y = \Delta t/\Delta y$ . Re-arranging equation (19) we can express the Godunov loss as:

$$\mathcal{L}_G := \frac{\omega}{N} \cdot \sum_{i,j,n} \left( \mathbf{Q}_{i,j}^{n+1} - \mathbf{Q}_{i,j}^n + \lambda_x \left[ \Delta \mathbf{F}(\mathfrak{R})_{i,j}^n \right] + \lambda_y \left[ \Delta \mathbf{G}(\mathfrak{R})_{i,j}^n \right] \right)^2, \quad (21)$$

where  $N$  is total number of points in space and time, and  $\omega$  weighs the residual contribution from each equation in a PDE system.

Riemann solvers mainly differ by how the fluxes  $\mathbf{F}(\mathfrak{R})$  and  $\mathbf{G}(\mathfrak{R})$  are estimated. To demonstrate the effectiveness of Godunov-type losses in our experiments, we use as an example the HLLC method to determine the intercell flux from the ML prediction. However, we emphasize that any Riemann flux estimator could be used instead. The HLLC method is outlined in Appendix B.

### 3 Experiments

#### 3.1 Experimental Setup

We examine the performance of the proposed Godunov-type loss in time-stepping the 2D Riemann problem at training and inference time. The 2D Riemann problem is a canonical problem in compressible fluid dynamics. A unit square domain  $[0, 1] \times [0, 1]$  is divided into four quadrants where each quadrant is uniformly initialized with its own set of  $(\rho, u, v, p)$ . The quadrants are numbered 1 to 4, anticlockwise from the top-right quadrant. The initialization of the quadrants determines the types of the four waves separating them. There are three wave types - rarefaction  $R$ , shock  $S$ , or contact  $J$ , characterized by their thermodynamic relations across the wave [50]. Given these relations there exist 19 physically admissible initial conditions representing different combinations of  $R$ ,  $J$ , and  $S$  [50]. These 19 configurations can be grouped into 6 classes characterized by numbers of each wave type:

$$4R \quad 4S \quad 4J \quad 2R + 2J \quad 2S + 2J \quad R + S + 2J$$

For the purposes of this paper we examine a representative configuration from each class:

$$R_{21}^+ R_{32}^+ R_{34}^+ R_{41}^+ \quad S_{21}^- S_{32}^+ S_{34}^+ S_{41}^- \quad J_{21}^- J_{32}^+ J_{34}^- J_{41}^+ \quad R_{21}^- J_{32}^- J_{34}^- R_{41}^- \quad S_{21}^+ J_{32}^+ J_{34}^+ S_{41}^+ \quad R_{21}^- J_{32}^- J_{34}^+ S_{41}^+$$

where subscript  $lr = \{21, 32, 34, 41\}$ . The thermodynamic relations across each wave type and the initialization values are outlined in Appendix C. For each of the six configurations, we train a Conv-LSTM model to time-step the initial condition at  $n = 0$  to  $n = 75$ , and then examine inference performance from  $n = 0$  to  $n = 125$ , where  $n = t/\Delta t$  and  $\Delta t = 0.002s$ . Training is performed in a series of fine-tunes which train 5 time-steps further than the previous fine-tune, using an Adam optimizer and a learning rate of  $\sim 10^{-5}$  throughout. We use a single convolutional layer to project the input with four channels (representing variables  $\rho, u, v, E$ ) to a representation with 128 channels. The model then time-steps this representation before projecting back to four channels using a deconvolutional layer. We use the swish activation owing to its ability in capturing sharp features compared to ReLU. Kaiming-initialization is used throughout. We implement this procedure with a Godunov-type loss  $\mathcal{L}_G$  as described in equation (21). For comparisons we repeat the procedure using regularized PDE-based PINN losses  $\mathcal{L}_{Visc}$  and  $\mathcal{L}_{TV+Ent}$ :

$$\mathcal{L}_{PDE} := \frac{\omega}{N} \cdot \|\partial_t \mathbf{Q} + \partial_x \mathbf{F} + \partial_y \mathbf{G}\|_2^2, \quad (22)$$

$$\mathcal{L}_{Visc} := \frac{\omega}{N} \cdot \|\partial_t \mathbf{Q} + \partial_x \mathbf{F} + \partial_y \mathbf{G} - \alpha (\partial_{xx} \mathbf{Q} + \partial_{yy} \mathbf{Q})\|_2^2, \quad (23)$$

$$\mathcal{L}_{TV+Ent} := \mathcal{L}_{PDE} + \frac{\beta_1}{N_t} \|\max(\mathbf{0}, \Delta TV)\|_2^2 + \frac{\beta_2}{N} \left\| \max\left(0, \partial_t \Phi + \partial_x \tilde{\mathbf{F}} + \partial_y \tilde{\mathbf{G}}\right) \right\|_2^2, \quad (24)$$

where  $N_t$  is the total number of points in time, and all derivatives in Equations (22), (23), and (24) are evaluated via 1st-order finite-differencing (again, we note that the L2 norms in equations (22) and (23) are taken over the space and time dimensions only).  $\mathcal{L}_{Visc}$  is an alternative way of obtaining entropy solutions by introducing artificial viscosity. The second term in  $\mathcal{L}_{TV+Ent}$  penalizes violations arising from oscillatory behaviour as measured by change in total variation [51]:

$$\Delta TV = \{TV^{n+1} - TV^n\}, \quad TV^n := \sum_{i,j} \Delta x |\mathbf{Q}_{i+1,j}^n - \mathbf{Q}_{i,j}^n| + \Delta y |\mathbf{Q}_{i,j+1}^n - \mathbf{Q}_{i,j}^n|. \quad (25)$$

The third term penalizes entropy condition violations where:

$$\Phi = -\rho \log\left(\frac{p}{\gamma \rho}\right), \quad \tilde{\mathbf{F}} = u\Phi, \quad \tilde{\mathbf{G}} = v\Phi. \quad (26)$$

We perform a grid-search and find  $\alpha = 0.0075$ ,  $\beta_1 = 100$ , and  $\beta_2 = 0.25$  give the best results for the regularized PINNs. We arbitrarily set all four elements of  $\omega$  to 0.25. We analyse performance of the three different losses  $\mathcal{L}_G$ ,  $\mathcal{L}_{TV+Ent}$ ,  $\mathcal{L}_{Visc}$  by comparing their models' predictions with respect to the solution of a reference 5th-order WENO numerical scheme [39]. The WENO ground truths are generated using the JAX-Fluids simulation framework [42]. The comparison is computed as percentage L2-norm difference between prediction and baseline.

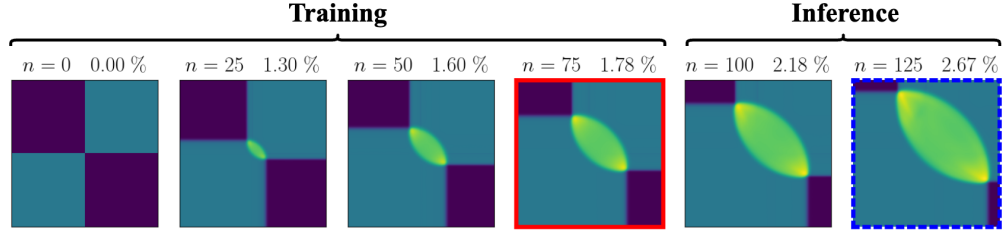


Figure 1: ML Predicted evolution of density for configuration  $S_{21}^- S_{32}^+ S_{34}^+ S_{41}^-$  (i.e. 4S) from  $n = 0$  to  $n = 125$ , for a Conv-LSTM model trained using Godunov-type loss  $\mathcal{L}_G$ . Numbers above each plot indicate time index and error with respect to a 5th-order WENO reference solution. Training is done over interval  $n = [0, 75]$ .

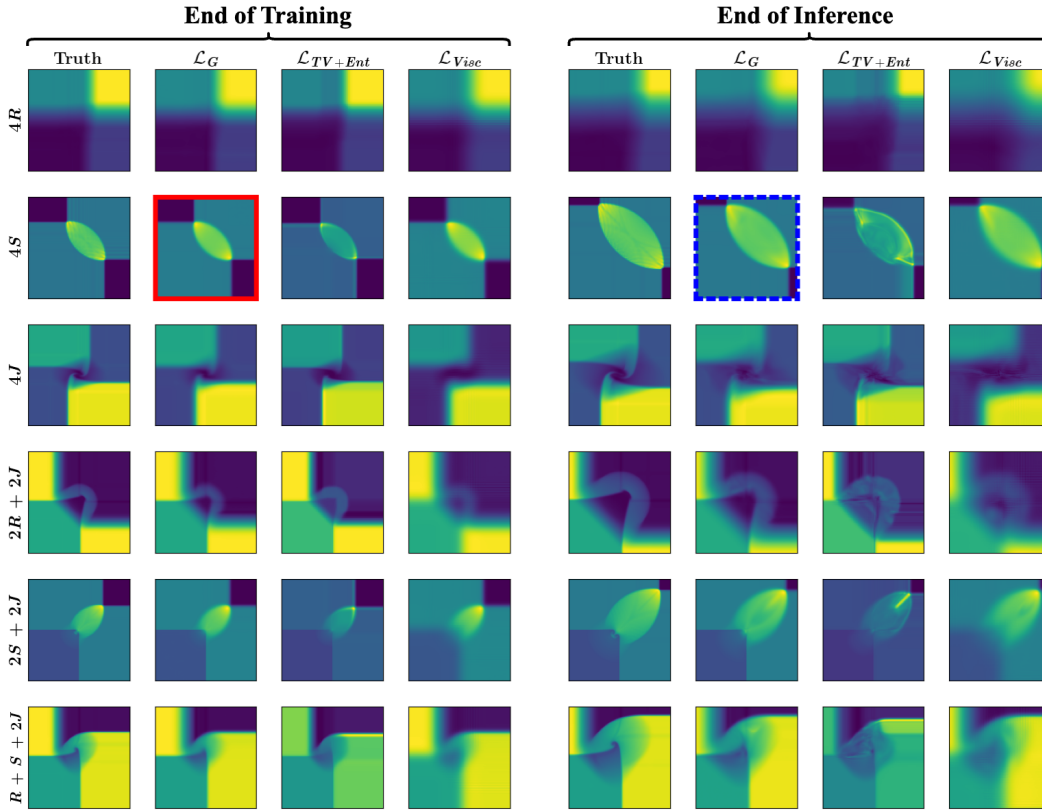


Figure 2: Predicted density fields by Conv-LSTMs trained with losses  $\mathcal{L}_G$ ,  $\mathcal{L}_{TV+Ent}$  and  $\mathcal{L}_{Visc}$ . Solutions shown are at end of training ( $n = 75$ ) and at end of inference ( $n = 125$ ), for the six configurations of interest. Ground truth solutions are obtained from a 5th-order WENO scheme.

### 3.2 Results and Discussion

Figure 1 shows the prediction of Conv-LSTM using Godunov-type loss  $\mathcal{L}_G$  for the case of four shock waves (4S). Error is 2.67% at  $n = 125$ , 50 time-steps past the training range. Figure 2 indicates the solution is visually faithful with respect to the WENO reference at end of training ( $n = 75$ ) and at end of inference ( $n = 125$ ), albeit slightly more diffusive. Also from Figure 2 we observe that the solution corresponding to  $\mathcal{L}_G$  is significantly less diffusive than that of the viscous loss  $\mathcal{L}_{Visc}$ . The solution using  $\mathcal{L}_{TV+Ent}$  appears to be slightly sharper at discontinuities compared to that of  $\mathcal{L}_G$  at  $n = 75$ , but upon closer inspection of its discontinuities we observe overshoots.  $\mathcal{L}_{TV+Ent}$  also

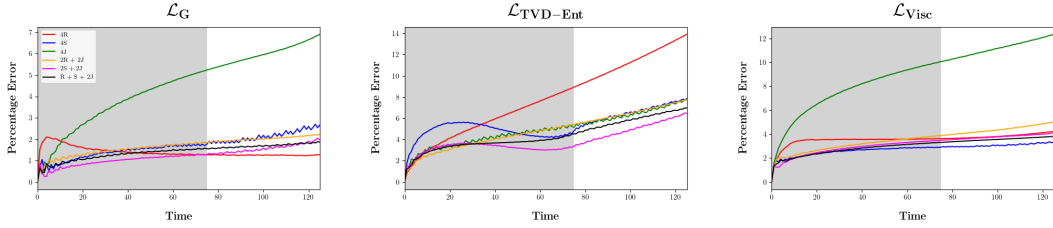


Figure 3: Error evolution of Conv-LSTMs trained with losses  $\mathcal{L}_G$ ,  $\mathcal{L}_{TV+Ent}$  and  $\mathcal{L}_{Visc}$ . Shaded region indicates training range ( $n = 0 - 75$ ). Ground truth solutions are obtained from a 5th-order WENO scheme.

Table 1: Error of Conv-LSTMs trained with  $\mathcal{L}_G$ ,  $\mathcal{L}_{TV+Ent}$  and  $\mathcal{L}_{Visc}$  at end of training ( $n = 75$ ) and at end of inference ( $n = 125$ ), for the six configurations of interest. The errors are computed as percentage L2-norm difference between ML predictions and WENO references.

CONFIGURATION	% ERROR ( $n = 75$ )			% ERROR ( $n = 125$ )		
	$\mathcal{L}_G$	$\mathcal{L}_{TV+Ent}$	$\mathcal{L}_{Visc}$	$\mathcal{L}_G$	$\mathcal{L}_{TV+Ent}$	$\mathcal{L}_{Visc}$
$4R$	<b>1.28</b>	8.95	3.62	<b>1.27</b>	13.92	4.23
$4S$	<b>1.78</b>	4.81	2.92	<b>2.67</b>	7.85	3.35
$4J$	5.23	<b>5.15</b>	10.08	<b>6.91</b>	7.75	12.36
$2R + 2J$	<b>1.83</b>	5.41	3.88	<b>2.23</b>	7.78	5.03
$2S + 2J$	<b>1.29</b>	3.39	3.49	<b>1.97</b>	6.47	4.06
$R + S + 2J$	<b>1.56</b>	4.53	3.31	<b>1.86</b>	6.97	3.81

performs poorly during inference as is apparent from Figure 2 and Table 1. Table 1 quantitatively shows  $\mathcal{L}_G$  outperforming the other losses for the case of  $4S$  at end of training and inference.

Similar trends are observed from Figure 2 and Table 1 for the other configurations: results from using  $\mathcal{L}_G$  are a) less diffusive compared to  $\mathcal{L}_{Visc}$ , b) of similar diffusivity compared to  $\mathcal{L}_{TV+Ent}$ , and c) the closest match to the WENO reference at both training and inference time. Performance of  $\mathcal{L}_{TV+Ent}$  and  $\mathcal{L}_{Visc}$  are notably poor at inference time. This may be due to  $\mathcal{L}_{TV+Ent}$  causing the model to be more prone to overfitting during training. A strong indicator that models using  $\mathcal{L}_{TV+Ent}$  are overfitting is that their corresponding solutions do not appear to be as evolved as the reference at  $n = 125$  - this lack of evolution is clear if we examine  $4S$  and  $2S + 2J$ , and in particular the position of the shock waves compared to the position of the same shock waves for the reference. This overfitting causes distortive artefacts to appear during inference - from Figure 2 this is particularly the case for all the configurations except  $4R$ .  $\mathcal{L}_{Visc}$  on the other hand is an already diffusive model at the end of training that further propagates diffusive behaviour in time causing loss of information - this is especially the case for  $2R + 2J$ . The disparity in performance between  $\mathcal{L}_G$  and the other losses is due to  $\mathcal{L}_G$  being more expressive of the problem that is to be solved in the sense that what is expected of the loss (monotonicity, entropy satisfaction) is inherently built into the loss without additional regularizing terms. The Godunov-type loss is derived from Godunov schemes, which have theoretical guarantees on entropy condition satisfaction and monotonicity. It is therefore expected to outperform regularized PINN-based losses that use finite differencing.

Figure 2 and Table 1 indicate that  $\mathcal{L}_G$  struggles most with the case of four contact waves ( $4J$ ). This could be due to the solution exhibiting a larger range of length scales compared to other configurations, because of the vorticity that evolves from the centre of the domain. As a result the model struggles to capture the finer feature of the vorticity towards the centre. Configuration  $R + S + 2J$  also appears to have this problem as apparent in Figure 2. A possible solution is to project to a greater number of channels before time-stepping. Alternatively, a multiscale model such as a U-Net could be adopted. Also of interest is that  $\mathcal{L}_{TV+Ent}$  marginally outperforms  $\mathcal{L}_G$  for configuration  $4J$  with the discontinuities being visibly sharper. Despite this,  $\mathcal{L}_G$  still extrapolates significantly better to  $n = 125$ .



## 4 Conclusion

In this paper we examine a Godunov-type loss function for modelling hyperbolic PDEs. We use this loss with a Conv-LSTM architecture to predict the evolution of the 2D Riemann problem under the influence of the 2D Euler equations. Results show high accuracy against a numerical reference and a generally superior and well-rounded performance compared to using PDE-based losses [17] with regularizations [41, 17]. This is due to the Godunov-type loss being inherently expressive of entropy and monotonicity constraints. The Godunov-type loss requires minimal hyperparameter tuning simplifying the search space for an optimized ML model. An obvious next step for this work is to extend it to the 3D Riemann problem or to approach a classical problem such as compressible flow past a cylinder. There is also scope to improve training stability of models that use Godunov-type losses. Incorporating reconstruction techniques into the architecture or loss for higher-order accuracy is another possible direction.

## References

- [1] Y. Bar-Sinai, S. Hoyer, J. Hickey, and M. P. Brenner, “Learning data-driven discretizations for partial differential equations,” *Proceedings of the National Academy of Sciences*, vol. 116, no. 31, pp. 15 344–15 349, 2019.
- [2] Z. Li, N. Kovachki, K. Aizzadenesheli, B. Liu, K. Bhattacharya, A. Stuart, and A. Anandkumar, “Fourier neural operator for parametric partial differential equations,” *arXiv preprint arXiv:2010.08895*, 2020.
- [3] D. Kochkov, J. A. Smith, A. Alieva, Q. Wang, M. P. Brenner, and S. Hoyer, “Machine learning–accelerated computational fluid dynamics,” *Proceedings of the National Academy of Sciences*, vol. 118, no. 21, p. e2101784118, 2021.
- [4] B. R. Noack, K. Afanasiev, M. MORZYŃSKI, G. Tadmor, and F. Thiele, “A hierarchy of low-dimensional models for the transient and post-transient cylinder wake,” *Journal of Fluid Mechanics*, vol. 497, pp. 335–363, 2003.
- [5] E. Kaiser, B. R. Noack, L. Cordier, A. Spohn, M. Segond, M. Abel, G. Daviller, J. Östh, S. Krajnović, and R. K. Niven, “Cluster-based reduced-order modelling of a mixing layer,” *Journal of Fluid Mechanics*, vol. 754, pp. 365–414, 2014.
- [6] T. Murata, K. Fukami, and K. Fukagata, “Nonlinear mode decomposition with convolutional neural networks for fluid dynamics,” *Journal of Fluid Mechanics*, vol. 882, p. A13, 2020.
- [7] J. Ling, A. Kurzawski, and J. Templeton, “Reynolds averaged turbulence modelling using deep neural networks with embedded invariance,” *Journal of Fluid Mechanics*, vol. 807, pp. 155–166, 2016.
- [8] J.-L. Wu, H. Xiao, and E. Paterson, “Physics-informed machine learning approach for augmenting turbulence models: A comprehensive framework,” *Physical Review Fluids*, vol. 3, no. 7, p. 074602, 2018.
- [9] A. Beck, D. Flad, and C.-D. Munz, “Deep neural networks for data-driven les closure models,” *Journal of Computational Physics*, vol. 398, p. 108910, 2019.
- [10] J. Rabault, F. Ren, W. Zhang, H. Tang, and H. Xu, “Deep reinforcement learning in fluid mechanics: A promising method for both active flow control and shape optimization,” *Journal of Hydrodynamics*, vol. 32, pp. 234–246, 2020.
- [11] K. Bieker, S. Peitz, S. L. Brunton, J. N. Kutz, and M. Dellnitz, “Deep model predictive flow control with limited sensor data and online learning,” *Theoretical and computational fluid dynamics*, vol. 34, pp. 577–591, 2020.
- [12] D. Bhattacharjee, B. Klose, G. B. Jacobs, and M. S. Hemati, “Data-driven selection of actuators for optimal control of airfoil separation,” *Theoretical and Computational Fluid Dynamics*, vol. 34, pp. 557–575, 2020.
- [13] K. Fukami, K. Fukagata, and K. Taira, “Super-resolution reconstruction of turbulent flows with machine learning,” *Journal of Fluid Mechanics*, vol. 870, pp. 106–120, 2019.
- [14] K. Fukami, B. An, M. Nohmi, M. Obuchi, and K. Taira, “Machine-learning-based reconstruction of turbulent vortices from sparse pressure sensors in a pump sump,” *Journal of Fluids Engineering*, vol. 144, no. 12, p. 121501, 2022.
- [15] D. Kelshaw, G. Rigas, and L. Magri, “Physics-informed cnns for super-resolution of sparse observations on dynamical systems,” *arXiv preprint arXiv:2210.17319*, 2022.
- [16] M. Raissi, P. Perdikaris, and G. E. Karniadakis, “Physics-informed neural networks: A deep learning framework for solving forward and inverse problems involving nonlinear partial differential equations,” *Journal of Computational physics*, vol. 378, pp. 686–707, 2019.
- [17] P. Ren, C. Rao, Y. Liu, J.-X. Wang, and H. Sun, “Phycrnet: Physics-informed convolutional-recurrent network for solving spatiotemporal pdes,” *Computer Methods in Applied Mechanics and Engineering*, vol. 389, p. 114399, 2022.

- [18] Z. Mao, A. D. Jagtap, and G. E. Karniadakis, “Physics-informed neural networks for high-speed flows,” *Computer Methods in Applied Mechanics and Engineering*, vol. 360, p. 112789, 2020.
- [19] L. Liu, S. Liu, H. Yong, F. Xiong, and T. Yu, “Discontinuity computing with physics-informed neural network,” *arXiv preprint arXiv:2206.03864*, 2022.
- [20] S. K. Godunov and I. Bohachevsky, “Finite difference method for numerical computation of discontinuous solutions of the equations of fluid dynamics,” *Matematičeskij sbornik*, vol. 47, no. 3, pp. 271–306, 1959.
- [21] E. F. Toro, *Riemann solvers and numerical methods for fluid dynamics: a practical introduction*. Springer Science & Business Media, 2013.
- [22] P. K. Sweby, “Godunov methods,” in *Godunov Methods: Theory and Applications*. Springer, 2001, pp. 879–898.
- [23] P. L. Roe, “Approximate riemann solvers, parameter vectors, and difference schemes,” *Journal of computational physics*, vol. 43, no. 2, pp. 357–372, 1981.
- [24] M. Pelanti, L. Quartapelle, and L. Vigevano, “A review of entropy fixes as applied to roe’s linearization,” *Teaching material of the Aerospace and Aeronautics Department of Politecnico di Milano*, p. 31, 2001.
- [25] B. Engquist and S. Osher, “One-sided difference approximations for nonlinear conservation laws,” *Mathematics of Computation*, vol. 36, no. 154, pp. 321–351, 1981.
- [26] S. Osher and F. Solomon, “Upwind difference schemes for hyperbolic systems of conservation laws,” *Mathematics of computation*, vol. 38, no. 158, pp. 339–374, 1982.
- [27] A. Harten, P. D. Lax, and B. v. Leer, “On upstream differencing and godunov-type schemes for hyperbolic conservation laws,” *SIAM review*, vol. 25, no. 1, pp. 35–61, 1983.
- [28] E. F. Toro, M. Spruce, and W. Speares, “Restoration of the contact surface in the hll-riemann solver,” *Shock waves*, vol. 4, pp. 25–34, 1994.
- [29] A. Harten, “High resolution schemes for hyperbolic conservation laws,” *Journal of computational physics*, vol. 135, no. 2, pp. 260–278, 1997.
- [30] B. Van Leer, “Towards the ultimate conservative difference scheme. iv. a new approach to numerical convection,” *Journal of computational physics*, vol. 23, no. 3, pp. 276–299, 1977.
- [31] —, “Towards the ultimate conservative difference scheme. v. a second-order sequel to godunov’s method,” *Journal of computational Physics*, vol. 32, no. 1, pp. 101–136, 1979.
- [32] P. Colella and P. R. Woodward, “The piecewise parabolic method (ppm) for gas-dynamical simulations,” *Journal of computational physics*, vol. 54, no. 1, pp. 174–201, 1984.
- [33] P. Woodward and P. Colella, “The numerical simulation of two-dimensional fluid flow with strong shocks,” *Journal of computational physics*, vol. 54, no. 1, pp. 115–173, 1984.
- [34] A. Harten, S. Osher, B. Engquist, and S. R. Chakravarthy, “Some results on uniformly high-order accurate essentially nonoscillatory schemes,” *Applied Numerical Mathematics*, vol. 2, no. 3-5, pp. 347–377, 1986.
- [35] A. Harten and S. Osher, “Uniformly high-order accurate nonoscillatory schemes. i,” *SIAM Journal on Numerical Analysis*, vol. 24, no. 2, pp. 279–309, 1987.
- [36] C.-W. Shu and S. Osher, “Efficient implementation of essentially non-oscillatory shock-capturing schemes,” *Journal of computational physics*, vol. 77, no. 2, pp. 439–471, 1988.
- [37] —, “Efficient implementation of essentially non-oscillatory shock-capturing schemes, ii,” *Journal of Computational Physics*, vol. 83, no. 1, pp. 32–78, 1989.
- [38] A. Harten, B. Engquist, S. Osher, and S. R. Chakravarthy, *Uniformly high order accurate essentially non-oscillatory schemes, III*. Springer, 1997.

- [39] X.-D. Liu, S. Osher, and T. Chan, “Weighted essentially non-oscillatory schemes,” *Journal of computational physics*, vol. 115, no. 1, pp. 200–212, 1994.
- [40] R. J. LeVeque, *Finite volume methods for hyperbolic problems*. Cambridge university press, 2002, vol. 31.
- [41] R. G. Patel, I. Manickam, N. A. Trask, M. A. Wood, M. Lee, I. Tomas, and E. C. Cyr, “Thermodynamically consistent physics-informed neural networks for hyperbolic systems,” *Journal of Computational Physics*, vol. 449, p. 110754, 2022.
- [42] D. A. Bezgin, A. B. Buhendwa, and N. A. Adams, “Jax-fluids: A fully-differentiable high-order computational fluid dynamics solver for compressible two-phase flows,” *Computer Physics Communications*, vol. 282, p. 108527, 2023.
- [43] S. Xiong, X. He, Y. Tong, R. Liu, and B. Zhu, “Roennets: Predicting discontinuity of hyperbolic systems from continuous data,” *arXiv preprint arXiv:2006.04180*, 2020.
- [44] T. Kossaczka, M. Ehrhardt, and M. Günther, “Enhanced fifth order weno shock-capturing schemes with deep learning,” *Results in Applied Mathematics*, vol. 12, p. 100201, 2021.
- [45] T. Kossaczka, A. D. Jagtap, and M. Ehrhardt, “Deep smoothness weno scheme for two-dimensional hyperbolic conservation laws: A deep learning approach for learning smoothness indicators,” *arXiv preprint arXiv:2309.10117*, 2023.
- [46] Y. Wang, Z. Shen, Z. Long, and B. Dong, “Learning to discretize: solving 1d scalar conservation laws via deep reinforcement learning,” *arXiv preprint arXiv:1905.11079*, 2019.
- [47] D. A. Bezgin, S. J. Schmidt, and N. A. Adams, “Weno3-nn: A maximum-order three-point data-driven weighted essentially non-oscillatory scheme,” *Journal of Computational Physics*, vol. 452, p. 110920, 2022.
- [48] Y. Li, L. Fu, and N. A. Adams, “A six-point neuron-based eno (eno6) scheme for compressible fluid dynamics,” *arXiv preprint arXiv:2207.08500*, 2022.
- [49] J. C.-H. Wang and J.-P. Hickey, “Fluxnet: a physics-informed learning-based riemann solver for transcritical flows with non-ideal thermodynamics,” *Computer Methods in Applied Mechanics and Engineering*, vol. 411, p. 116070, 2023.
- [50] C. W. Schulz-Rinne, “Classification of the riemann problem for two-dimensional gas dynamics,” *SIAM journal on mathematical analysis*, vol. 24, no. 1, pp. 76–88, 1993.
- [51] L. Krivodonova and A. Smirnov, “On the tvd property of second order methods for 2d scalar conservation laws,” 2021.
- [52] S. Hochreiter and J. Schmidhuber, “Long short-term memory,” *Neural computation*, vol. 9, no. 8, pp. 1735–1780, 1997.
- [53] E. F. Toro, “The hllc riemann solver,” *Shock Waves*, vol. 29, no. 8, pp. 1065–1082, 2019.
- [54] S. Davis, “Simplified second-order godunov-type methods,” *SIAM Journal on Scientific and Statistical Computing*, vol. 9, no. 3, pp. 445–473, 1988.
- [55] A. Kurganov and E. Tadmor, “Solution of two-dimensional riemann problems for gas dynamics without riemann problem solvers,” *Numerical Methods for Partial Differential Equations: An International Journal*, vol. 18, no. 5, pp. 584–608, 2002.

## A Convolutional LSTM

We implement a convolutional LSTM architecture with a global residual connection to mimic the forward Eulerian scheme:

$$\mathbf{X}^{n+1} = \mathbf{X}^n + \Delta\mathbf{X}^n = \mathbf{X}^n + \Delta t \cdot \mathcal{F}(\mathbf{X}^n; \Theta) \quad (27)$$

where  $\mathbf{X}$  is the feature,  $\mathcal{F}$  is the network parameterized by  $\Theta$ ,  $\Delta t$  is the step size, and  $n$  is the temporal index. The network  $\mathcal{F}$  comprises an encoder-LSTM-decoder combination ( $\mathcal{F}_{Enc}$ ,  $\mathcal{F}_{LSTM}$ ,  $\mathcal{F}_{Dec}$ ):

$$\bar{\mathbf{X}}^n = \mathcal{F}_{Enc}(\mathbf{X}^n; \Theta_{Enc}) \quad (28)$$

$$\mathbf{h}^n = \mathcal{F}_{LSTM}(\bar{\mathbf{X}}^n, \mathbf{h}^{n-1}, \mathbf{C}^{n-1}; \Theta_{LSTM}) \quad (29)$$

$$\Delta\mathbf{X}^n = \Delta t \cdot \mathcal{F}_{Dec}(\mathbf{h}^n; \Theta_{Dec}) \quad (30)$$

where  $\bar{\mathbf{X}}$  is the encoding of  $\mathbf{X}$ ,  $\mathbf{h}$  is the hidden state and  $\mathbf{C}$  is the cell state. The LSTM module  $\mathcal{F}_{LSTM}$  comprises an input gate  $\mathbf{i}$ , forget gate  $\mathbf{f}$ , and output gate  $\mathbf{o}$ , parameterized by weights  $\{\mathbf{W}_i, \mathbf{W}_f, \mathbf{W}_c, \mathbf{W}_o\}$  and biases  $\{\mathbf{b}_i, \mathbf{b}_f, \mathbf{b}_c, \mathbf{b}_o\}$ . Equations 31 - 36 outline the LSTM operations [52]:

$$\mathbf{i}^n = \sigma(\mathbf{W}_i * [\bar{\mathbf{X}}^n, \mathbf{h}^{n-1}] + \mathbf{b}_i) \quad (31)$$

$$\mathbf{f}^n = \sigma(\mathbf{W}_f * [\bar{\mathbf{X}}^n, \mathbf{h}^{n-1}] + \mathbf{b}_f) \quad (32)$$

$$\tilde{\mathbf{C}}^{n-1} = \tanh(\mathbf{W}_c * [\bar{\mathbf{X}}^n, \mathbf{h}^{n-1}] + \mathbf{b}_c) \quad (33)$$

$$\mathbf{C}^n = \mathbf{f}^n \odot \mathbf{C}^{n-1} + \mathbf{i}^n \odot \tilde{\mathbf{C}}^{n-1} \quad (34)$$

$$\mathbf{o}^n = \sigma(\mathbf{W}_o * [\bar{\mathbf{X}}^n, \mathbf{h}^{n-1}] + \mathbf{b}_o) \quad (35)$$

$$\mathbf{h}^n = \mathbf{o}^n \odot \tanh(\mathbf{C}^n) \quad (36)$$

where  $\sigma$  is the sigmoid function,  $*$  is the convolutional operation, and  $\odot$  is the Hadamard product.

## B HLLC Flux

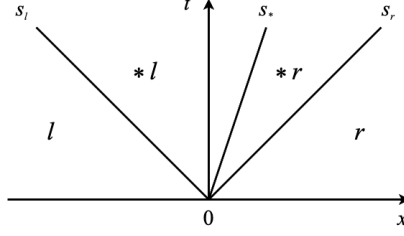


Figure 4: The three-wave model assumed by the HLLC solver. The left and right characteristic lines correspond to the fastest and slowest signals,  $s_l$  and  $s_r$ , emerging from the cell interface at  $x = 0$ . The middle characteristic corresponds to the wave of speed  $s_*$  which accounts for contact and shear waves.

An outline of the HLLC algorithm is now presented. In order to determine the HLLC flux normal to a cell interface for the 2D Euler equations, it is sufficient to consider a  $x$ -split version of the 2D Euler equations because of rotational invariance [53]:

$$\partial_t \begin{pmatrix} \rho \\ \rho u \\ \rho v \\ E \end{pmatrix} + \partial_x \begin{pmatrix} \rho u \\ \rho u^2 + p \\ \rho uv \\ u(E + p) \end{pmatrix} = \mathbf{0} \quad (37)$$

Given this, we then estimate the pressure in the star region  $\bar{p}_*$ . A reliable approximation is [53]:

$$\bar{p}_* = \left[ \frac{a_l + a_r - \frac{\gamma-1}{2}(u_r - u_l)}{\frac{a_l}{p_l^z} + \frac{a_r}{p_r^z}} \right]^{1/z} \quad (38)$$

where  $a = \sqrt{\gamma p / \rho}$  is the speed of sound and  $z = (\gamma - 1) / 2\gamma$ . Wave speeds  $s_l$  and  $s_r$  are then estimated as [54, 53]:

$$s_l = u_l - a_l q_l, \quad s_r = u_r + a_r q_r, \quad q_k = \begin{cases} 1 & \text{if } \bar{p}_* \leq p_k, \\ \left[ 1 + \left( \frac{\gamma+1}{2\gamma} \right) \left( \frac{\bar{p}_*}{p_k} - 1 \right) \right]^{\frac{1}{2}} & \text{if } \bar{p}_* > p_k \end{cases} \quad (39)$$

where  $k = \{l, r\}$ . We then use  $s_l$  and  $s_r$  to compute intermediate speed  $s_*$  [53]:

$$s_* = \frac{p_r - p_l + \rho_l u_l (s_l - u_l) - \rho_r u_r (s_r - u_r)}{\rho_l (s_l - u_l) - \rho_r (s_r - u_r)}. \quad (40)$$

The intermediate conservative vectors  $\mathbf{Q}_{*l}$  and  $\mathbf{Q}_{*r}$  are then computed using  $s_*$ ,  $s_l$  and  $s_r$  as [53]:

$$\mathbf{Q}_{*k} = \rho_k \begin{pmatrix} \frac{s_k - u_k}{s_k - s_*} \\ \frac{E_k}{\rho_k} + (s_* - u_k) \left[ s_* + \frac{p_k}{\rho_k (s_k - u_k)} \right] \end{pmatrix}. \quad (41)$$

Finally, the intermediate flux vectors  $\mathbf{F}_{*l}$  and  $\mathbf{F}_{*r}$  are computed from the state vectors so that the flux  $\mathbf{F}_{i+\frac{1}{2}}^n$  is computed using equation (42).

$$\mathbf{F}_{*k} = \mathbf{F}_k + s_k (\mathbf{Q}_{*k} - \mathbf{Q}_k), \quad \mathbf{F}_{i+\frac{1}{2}}^n = \begin{cases} \mathbf{F}_l & 0 \leq s_l, \\ \mathbf{F}_{*l} & s_l \leq 0 \leq s_*, \\ \mathbf{F}_{*r} & s_* \leq 0 \leq s_r, \\ \mathbf{F}_r & 0 \geq s_r. \end{cases} \quad (42)$$

Due to rotational invariance, an analogous procedure allows us to determine the flux  $\mathbf{G}_{j+\frac{1}{2}}^n$ .

## C Initialization of 2D Riemann Configurations

A unit square domain  $[0, 1] \times [0, 1]$  is divided into four quadrants where each quadrant is uniformly initialized with its own set of  $\mathbf{X} = (\rho, u, v, E)$ . The quadrants are numbered 1 to 4, anticlockwise from the top-right quadrant. The initialization of the quadrants determines the types of the four waves separating them. There are three wave types - rarefaction  $R$ , shock  $S$ , or contact  $J$ , characterized by their thermodynamic relations across the wave [50]:

$$R_{lr}^{\pm} : w_l - w_r = \pm \frac{2\sqrt{\gamma}}{\gamma - 1} \left( \sqrt{\frac{p_l}{\rho_l}} - \sqrt{\frac{p_r}{\rho_r}} \right), \quad \frac{p_l}{p_r} = \left( \frac{\rho_l}{\rho_r} \right)^{\gamma}, \quad w'_l = w'_r, \quad (43)$$

$$S_{lr}^{\pm} : \frac{w_l - w_r}{\rho_r - \rho_l} = \pm \sqrt{\frac{1}{\rho_r \rho_l} \frac{p_r - p_l}{\rho_r - \rho_l}}, \quad \frac{\rho_l}{\rho_r} = \frac{(\gamma + 1)\rho_l - (\gamma - 1)\rho_r}{(\gamma + 1)\rho_r - (\gamma - 1)\rho_l}, \quad w'_l = w'_r, \quad (44)$$

$$J_{lr}^{\pm} : \text{sgn}(w'_r - w'_l) = \pm 1, \quad w_l = w_r, \quad p_l = p_r, \quad (45)$$

$$E := \frac{1}{2} (u^2 + v^2) + \frac{p}{\rho(\gamma - 1)}, \quad (46)$$

where subscript  $lr = \{21, 32, 34, 41\}$ ,  $w$  and  $w'$  are the normal and tangential velocities (w.r.t waves). The following are the initialization values of the 2D Riemann configurations explored in this work.

$$R_{21}^+ R_{32}^+ R_{34}^+ R_{41}^+ := \begin{cases} \mathbf{X}_1 = (1.0000, & 0.0000, & 0.0000, & 2.5000), & x > 0.5, & y > 0.5 \\ \mathbf{X}_2 = (0.5197, & -0.7259, & 0.0000, & 2.1877), & x < 0.5, & y > 0.5 \\ \mathbf{X}_3 = (0.1072, & -0.7259, & -1.4045, & 2.2736), & x < 0.5, & y < 0.5 \\ \mathbf{X}_4 = (0.2579, & 0.0000, & -1.4045, & 2.4404), & x > 0.5, & y < 0.5 \end{cases}$$

$$S_{21}^- S_{32}^+ S_{34}^+ S_{41}^- := \begin{cases} \mathbf{X}_1 = (1.1000, & 0.0000, & 0.0000, & 2.5000), & x > 0.5, & y > 0.5 \\ \mathbf{X}_2 = (0.5065, & 0.8939, & 0.0000, & 2.1271), & x < 0.5, & y > 0.5 \\ \mathbf{X}_3 = (1.1000, & 0.8939, & 0.8939, & 3.2991), & x < 0.5, & y < 0.5 \\ \mathbf{X}_4 = (0.5065, & 0.0000, & 0.8939, & 2.1271), & x > 0.5, & y < 0.5 \end{cases}$$

$$J_{21}^- J_{32}^+ J_{34}^- J_{41}^+ := \begin{cases} \mathbf{X}_1 = (1.0000, & 0.7500, & -0.5000, & 2.9063), & x > 0.5, & y > 0.5 \\ \mathbf{X}_2 = (2.0000, & 0.7500, & 0.5000, & 1.6563), & x < 0.5, & y > 0.5 \\ \mathbf{X}_3 = (1.0000, & -0.7500, & 0.5000, & 2.9063), & x < 0.5, & y < 0.5 \\ \mathbf{X}_4 = (3.0000, & -0.7500, & -0.5000, & 1.2396), & x > 0.5, & y < 0.5 \end{cases}$$

$$R_{21}^- J_{32}^- J_{34}^- R_{41}^- := \begin{cases} \mathbf{X}_1 = (0.5197, & 0.1000, & 0.1000, & 1.9342), & x > 0.5, & y > 0.5 \\ \mathbf{X}_2 = (1.0000, & -0.6259, & 0.1000, & 2.7009), & x < 0.5, & y > 0.5 \\ \mathbf{X}_3 = (0.8000, & 0.1000, & 0.1000, & 3.1350), & x < 0.5, & y < 0.5 \\ \mathbf{X}_4 = (1.0000, & 0.1000, & -0.6259, & 2.7009), & x > 0.5, & y < 0.5 \end{cases}$$

$$S_{21}^+ J_{32}^+ J_{34}^+ S_{41}^+ := \begin{cases} \mathbf{X}_1 = (0.5313, & 0.0000, & 0.0000, & 1.8822), & x > 0.5, & y > 0.5 \\ \mathbf{X}_2 = (1.0000, & 0.7276, & 0.0000, & 2.7647), & x < 0.5, & y > 0.5 \\ \mathbf{X}_3 = (0.8000, & 0.0000, & 0.0000, & 3.1250), & x < 0.5, & y < 0.5 \\ \mathbf{X}_4 = (1.0000, & 0.0000, & 0.7276, & 2.7647), & x > 0.5, & y < 0.5 \end{cases}$$

$$R_{21}^- J_{32}^- J_{34}^+ S_{41}^+ := \begin{cases} \mathbf{X}_1 = (0.5313, & 0.1000, & 0.1000, & 1.8922), & x > 0.5, & y > 0.5 \\ \mathbf{X}_2 = (1.0222, & -0.6179, & 0.1000, & 2.6416), & x < 0.5, & y > 0.5 \\ \mathbf{X}_3 = (0.8000, & 0.1000, & 0.1000, & 3.1350), & x < 0.5, & y < 0.5 \\ \mathbf{X}_4 = (1.0000, & 0.1000, & 0.8276, & 2.8475), & x > 0.5, & y < 0.5 \end{cases}$$

For initialization values of other 2D Riemann configurations, see Kurganov and Tadmor [55].